J Mater Sci (2022) 57:11748–11760

Composites & nanocomposites

The effect of deformation parameters on the dynamic recrystallization and microstructure evolution of the quasi-continuous network reinforced TiAl/B_4C composites

Juan Li[1], Mingao Li[1,2,3,*], Tao Zhou[1,*], Li Hu[1], Laixin Shi[1], Shulong Xiao[2,3], Yuyong Chen[2,3], and Lijuan Xu[3]

[1] School of Materials Science and Engineering, Chongqing University of Technology, Chongqing 400054, People's Republic of China
[2] National Key Laboratory of Science and Technology on Precision Heat Processing of Metals, Harbin Institute of Technology, Harbin 150001, People's Republic of China
[3] School of Materials Science and Engineering, Harbin Institute of Technology, Harbin 150001, People's Republic of China

Received: 13 February 2022
Accepted: 30 May 2022
Published online: 20 June 2022

ABSTRACT

Dynamic recrystallization mechanism and microstructure evolution of a novel quasi-continuous network reinforced TiAl matrix composites, TiAl/B_4C composites were studied in this paper. The isothermal compression experiments, the scanning electron microscopy, and the electron back-scattered diffraction were carried out. Besides the discontinuous dynamic recrystallization (DDRX), the continuous dynamic recrystallization occurred in γ-phase grains during the loading, characterized by crystal orientation accumulation. Additionally, a large number of $89 \pm 3°$ grain boundaries associated with DDRX also appeared during the loading. With the temperature increasing or/and the strain rate decreasing, the volume fraction of recrystallized grains increased significantly, the $< 010 >$ crystal direction of γ-phase grains within the matrix unit of present composites was gradually parallel to compression direction, and the texture changed from scatter to concentration. The variety of texture was mainly related to different dynamic recrystallization mechanisms in various conditions.

Handling Editor: Catalin Croitoru.

Address correspondence to E-mail: limingao@cqut.edu.cn; zt19811118@cqut.edu.cn

https://doi.org/10.1007/s10853-022-07396-1

Introduction

Due to excellent oxidation resistance and strength at high temperatures, high specific strength, and low density, TiAl matrix composites are thought as the primary candidate to replace Ni-based superalloys and to achieve large-scale weight reduction in the aerospace engine [1, 2]. However, high-temperature strength or room-temperature plasticity of the existing TiAl matrix composites were insufficient to meet the requirement of structural materials with high performance [2–4]. Thus, some researchers tried to improve the mechanical properties of TiAl matrix composites by different types of reinforcement addition, such as Ti_2AlNb [5], Ti_2AlN [6, 7], Y_2O_3 [8, 9], Ti_3AlC [10], Ti_2AlC [11], and TiB [12], etc. Meanwhile, growth and distribution of reinforcements were controlled to establish a quasi-continuous network structure within TiAl matrix composites, for excellent mechanical properties [6, 11, 13].

Wang et al. [6] established a quasi-continuous network reinforced structure with Ti_2AlN particles within TiAl matrix composites through the in-situ reaction of nitrogen with titanium and aluminum. The authors enhanced the flexural strength of the materials at 700 °C and 800 °C, but the flexural strength decreased significantly with the temperature increasing to 900 °C. Ren et al. [11] prepared Ti_2AlC/TiAl composites with a three-dimensional network structure and increased the flexural strength of the composite with 20 vol% Ti_2AlC to 900.9 MPa at room temperature. In combination with pressure infiltration and hot-press sintering, Li et al. [13] prepared TiAl-based composites with a quasi-continuous network structure consisting of Ti_5Si_3 reinforcement. The authors increased the ultimate tensile strength (UTS) of the composites at 700 °C and 800 °C and the elongation at room temperature to 594 MPa, 520 MPa, and 2.5%, respectively, but the UTS of the composites at 850 °C was only 390 MPa.

Based on above researches, the authors tend to establish a quasi-continuous network reinforced structure within TiAl matrix composites, for the improvements of mechanical properties. Li et al. [10] found that carbides with self-lubricating properties could coordinate the plastic deformation of TiAl matrix through activated slipping systems during the loading, and the refined α_2/γ lamellae spacing caused by carbon addition could support creep deformation of TiAl alloys. Meanwhile, borides could effectively enhanced the UTS of TiAl alloys through the obstacles for dislocation movement and pinning interfaces sliding at high temperature [12]. Thus, a novel quasi-continuous network reinforced structure with in-situ borides and carbides was constructed at the interface layer of matrix unit within TiAl-based composites. Borides and carbides were employed to strengthen the interface layer of matrix units. Furthermore, hot processing is treated as an important manufacture for TiAl matrix composites in the aerospace industry. Deformation behavior and microstructure evolution of the novel TiAl matrix composites with quasi-continuous network reinforced structures are still not investigated clearly, which hinder the application of present composites. Thus, it is necessary to study deformation behavior and microstructure evolution of the composites before industrial practice.

The main objective is to investigate the effect of temperature and strain rate on the microstructure evolution and the deformation behavior of the novel TiAl/B_4C composites in this paper. The microstructure evolution will be analyzed by scanning electron microscopy (SEM), electron back-scattered diffraction (EBSD), and X-ray diffraction (XRD).

Materials and methods

TiAl (Ti–45Al–8Nb at%) powders and 5.75 wt% B_4C powders were used to fabricate TiAl/B_4C composites with quasi-continuous network reinforced structure via vacuum reactive hot-press sintering technique, as exhibited in Fig. 1. As shown in Fig. 2a–f, B_4C powders displayed an average diameter of 5 μm. TiAl powders with an average diameter of 120 μm mainly consisted of α_2-Ti_3Al phase and γ-TiAl phase. A low-

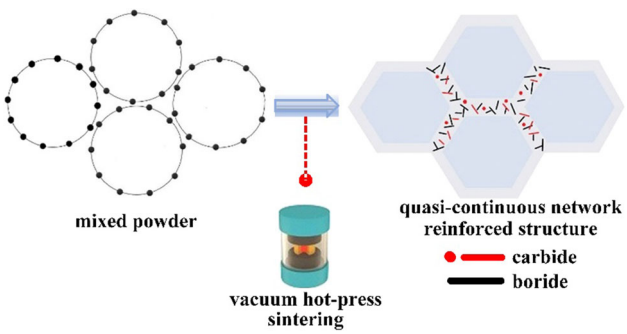

Figure 1 The fabrication process of the quasi-continuous network reinforced TiAl/B4C composites.

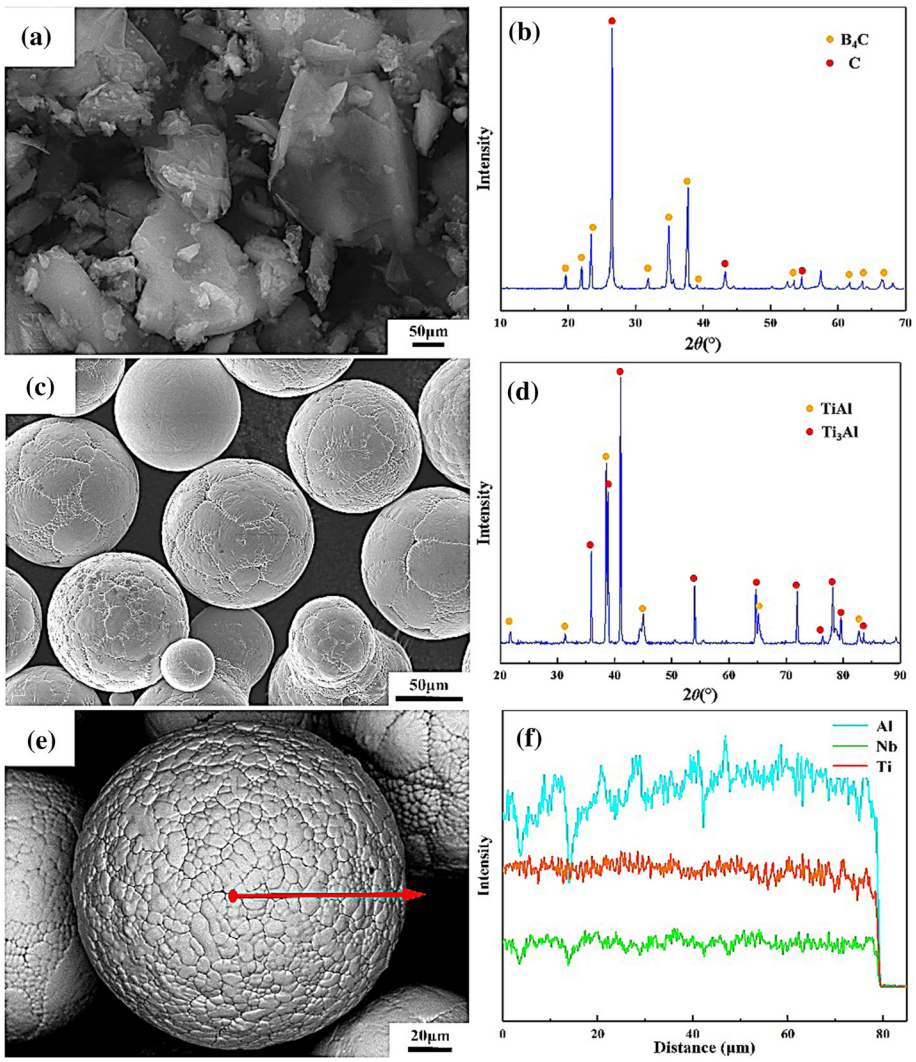

Figure 2 The SEM images and XRD patterns of powders: **a** SEM images and **b** XRD pattern of B4C powders; **c** SEM images and **d** XRD pattern of TiAl powders; **e**–**f** Line scanning analysis.

energy ball milling was used to combine TiAl powders and B_4C powders in argon atmosphere; the mixing speed and the duration of low-energy ball milling in this work were 200 rpm and 8 h. Vacuum hot pressing sintering was used to compact the mixed powder in a graphite mold at 1200 °C for 1 h and under a pressure of 40 MPa. After hot pressing sintering, the samples were held at 900 °C for 12 h and then furnace quenched.

The specimens with Φ8 mm × 12 mm were used in isothermal compression tests, which were carried out in Gleeble-3500 instrument. Deformation conditions were chosen to be (1050 °C, 1150 °C)/0.01 s^{-1} and 1150 °C/(0.1 s^{-1}, 0.001 s^{-1}); heating rate was 10 °C/s; engineering strain was 50%. After isothermal compression, the samples were immediately water quenched to preserve deformed microstructure. An X-ray diffractometer with Cu Kα radiation was used to determine the phase composition of raw material powders and sintered composites with steps of 0.013° and scanning angles of 10–90°. Scanning electron microscopy (SEM) and electron back-scattered diffraction (EBSD) techniques were used to analyze microstructure. Samples for EBSD analysis were electrochemically polished with a solution of 10% perchloric acid, 30% butanol, and 60% methanol at approximately −25 °C and 25 V. EBSD observation was carried out with the step of 0.15 μm. In this work, the crystallographic information of gamma phase with FCT structure was entered in the Twist module of Channel 5 software, to establish EBSP file of gamma phase for EBSD analysis.

Results and discussion

The initial microstructure of TiAl/B_4C composites

The SEM images and XRD pattern of TiAl/B_4C composites are exhibited in Fig. 3. The initial microstructure of the composite is shown in Fig. 3f. The present composite mainly consists of γ-TiAl, α_2-Ti_3Al, TiB_2, and Ti_2AlC. No peak of B_4C in the XRD pattern indicates that borides and carbides reinforcements synthesize completely during the hot-press sintering process. The initial as-sintered microstructure of TiAl/B_4C composites is shown in Fig. 3a–e. The ($\alpha_2 + \gamma$) lamellae can be observed in matrix unit; the average size of lamellar colonies on the edge of matrix unit is much smaller than that in the center because the cooling rate of external powder is fast. To better exhibit the arrangement of the reinforcements at the interface layer, the sample was etched for various time. Figure 3e shows the sample etched at long time (10 min), which caused the matrix unit to be etched completely. As shown in Fig. 3a–e, borides and carbides distributed at the interface of matrix units and constructed a quasi-continuous network reinforced structure.

Deformation behavior

Hot process of TiAl composites is mainly affected by work hardening, dynamic recrystallization, and dynamic recovery. Due to low stacking fault energy, the softening process of TiAl alloys mainly depends on dynamic recrystallization during the loading [14]. Temperatures and strain rates significantly influence the dynamic recrystallization of TiAl matrix composites during the loading. To study the effect of deformation parameters on the deformation behavior of TiAl/B_4C composites, the flow stress curves in

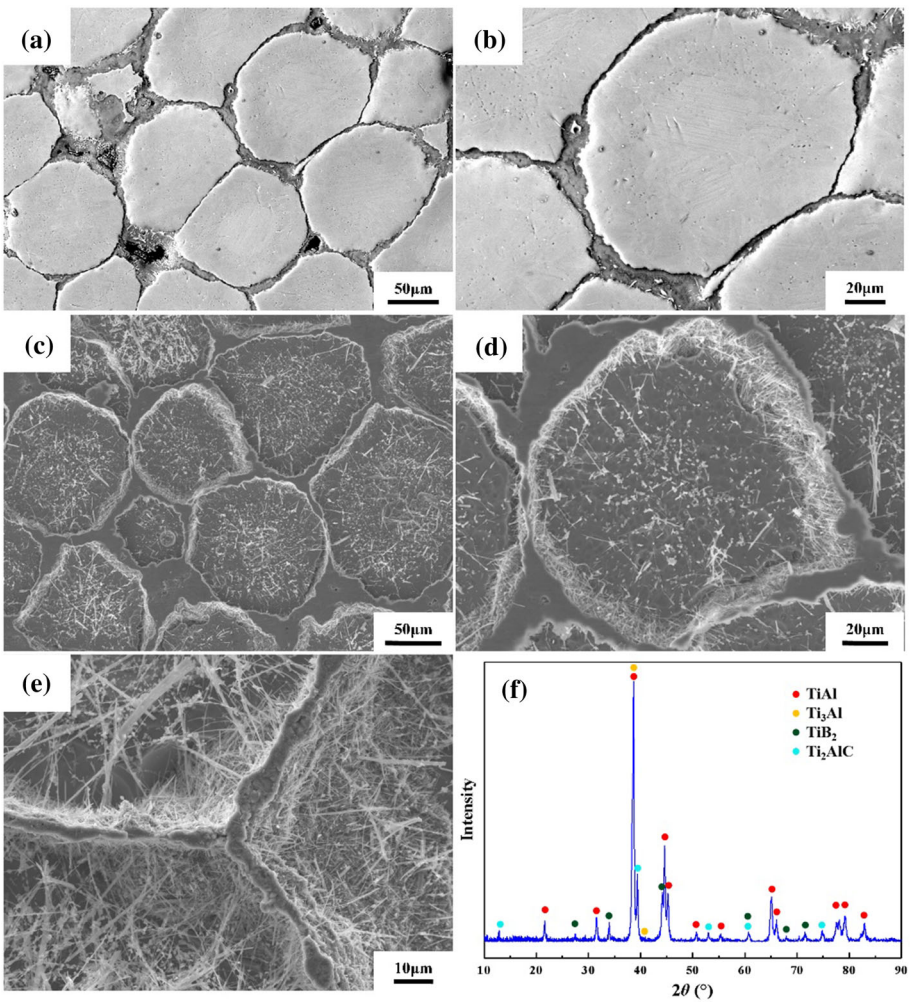

Figure 3 The initial microstructure of the quasi-continuous network reinforced TiAl/B4C composites: **a, b** BSE image; **c–e** SE image; **f** X-ray diffraction pattern.

various conditions (1050 °C/0.01 s^{-1} and 1150 °C/0.01 s^{-1}) are exhibited in Fig. 4.

It can be observed that flow stress increases rapidly to peak during the initial stage, and then decreases gradually, finally tends to be stable. The phenomenon is due to the work hardening caused by dislocation pile-ups in the initial deformation stage, which leads to a significant increase in flow stress. Dislocation pile-ups will promote the nucleation of recrystallized grains during the loading. When work hardening and recrystallization reach equilibrium, flow stress reaches the peak stress. With further deformation, the effect of recrystallization is stronger than that of work hardening, and flow stress decreases gradually. When recrystallization and work hardening reach equilibrium again, the flow stress curve becomes stable. As shown in Fig. 4a and b, the flow stress decreases with temperature increasing or/and strain rate decreasing.

Microstructure evolution during the isothermal compression

Based on the stress–strain curves, the variety of temperature and strain rate can influence microstructure evolution of the present TiAl matrix composites. TiAl-based materials display different types of microstructure evolution in various condition, which influences mechanical properties [15, 16]. As shown in Fig. 5, the reinforcements in the interfaces rotate in the direction that is perpendicular to compressive direction, while matrix units tend to deform along the compressive direction during the loading. Furthermore, it can also be seen that the thick lamellar colonies in the center of the matrix unit are bent and twisted in condition 1050 °C/0.01 s^{-1} and 1150 °C/0.1 s^{-1}. Moreover, $(\alpha_2 + \gamma)$ lamellar colonies coarsen substantially as a result of dynamic recrystallization at high temperatures. The recrystallized grains can be seen clearly in the BC diagram. In condition 1050 °C/0.01 s^{-1} and 1150 °C/0.1 s^{-1}, recrystallized grains distribute as necklace-like around the deformed grains. The recrystallized grains display much larger size in condition 1150 °C/0.01 s^{-1} and 1150 °C/0.001 s^{-1}, compared to that in condition 1050 °C/0.01 s^{-1} and 1150 °C/0.1 s^{-1}. High deformation temperature and sufficient time can promote dislocation slipping and the nucleation and growth of recrystallized grains.

Dynamic recrystallization mechanism

The nucleation and growth of recrystallized γ grains dominate the deformation of matrix units. As shown in Fig. 6, the grain boundary and GOS distribution of γ-phase can be seen. As the note in the figures, significant differences are exhibited in the GOS values of individual samples. Previous studies have suggested that the end-point of first considerable peak with a low GOS value could be regarded as the critical GOS value (CGV) of recrystallized grains [17–19]. As shown in Fig. 6e–h, the CGV values of the four samples are 2.1, 1.6, 2.1, and 1.3, while the volume fractions of recrystallized grains are 37%, 33%, 18.4%, and 39.3%, respectively. The size of recrystallized grains in condition 1150 °C/0.01 s^{-1} is about 1.98 μm, which is 50% larger than that in condition 1050 °C/0.01 s^{-1}. The size of recrystallized grains in condition 1150 °C/0.001 s^{-1} is 70% larger than that in condition 1150 °C/0.1 s^{-1}.

Figure 6a–d shows the grain boundary diagram of γ phase in different conditions. Low angle grain boundaries (LAGBs, 2–10°), medium angle grain boundaries (MAGBs, 10–15°), and high angle grain boundaries (HAGBs, 15–180°) are marked with green, red, and blue lines. HAGBs are generally produced

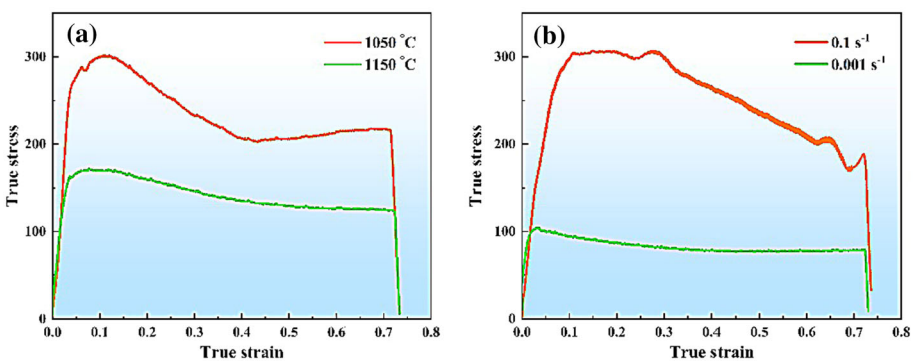

Figure 4 The flow stress curves of the quasi-continuous network reinforced TiAl/B4C composites in different conditions **a** 0.01 s^{-1}, **b** 1150 °C.

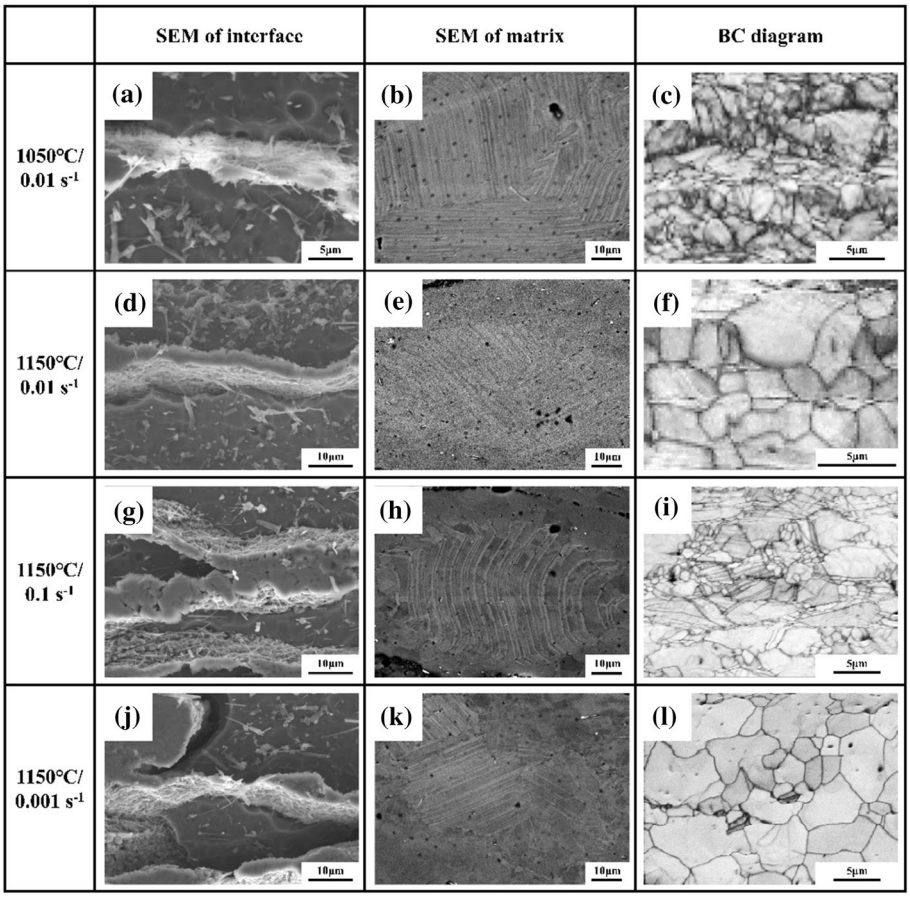

Figure 5 The SEM images of the interfaces **a**, **d**, **g**, **j** and matrix **b**, **e**, **h**, **k**, the BC diagram **c**, **f**, **i**, **l** of γ phase within the quasi-continuous network reinforced TiAl composites in various conditions.

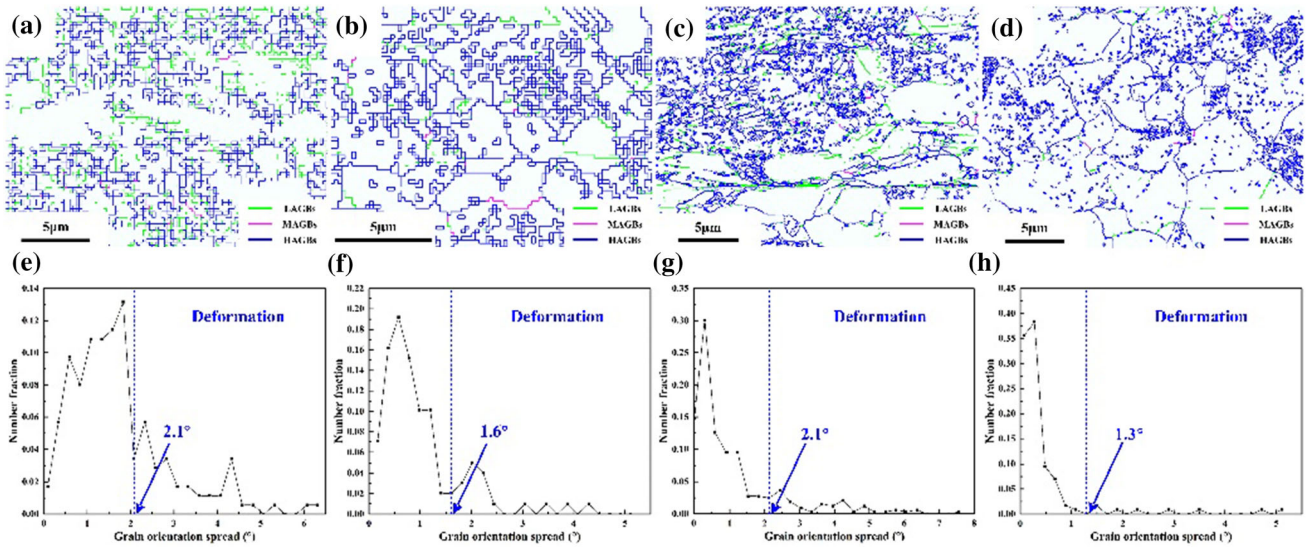

Figure 6 Grain boundary **a**–**d** and GOS **e**–**h** distribution of γ phase after compressive deformation in condition 1050 °C/0.01 s^{-1} **a**, **e**,1150 °C/0.01 s^{-1} **b**, **f**,1150 °C/0.1 s^{-1} **c**, **g** and 1150 °C/0.001 s^{-1} **d**, **f**.

by recrystallized grains nucleation or/and grain coarsening, while LAGBs usually form in the sub-grain boundaries during the loading. In Fig. 6a and b, a large number of LAGBs extend to the region of grain center and exist within the deformed grains. The LAGBs split deformed grains into interconnected

parts, which indicates the appearance of sub-grains within the deformed grains. In addition, MAGBs can also be seen in the diagram, which is traditionally regarded as a prerequisite for the nucleation of CDRXed grains. Thus, it is judged that CDRX displays an important influence on the deformation process [20].

Figure 7 shows the misorientation angle distribution of γ phase in different samples. It can be clearly seen that there is a dominant angle peak with 89 ± 3° misorientation. The 89 ± 3° GBs are marked with a red line in the GOS maps. It can be seen that the GOS values of the grains with 89 ± 3°GBs are less than the CGV values of the corresponding samples. These grains are judged as DRX grains. Most of these types of grains nucleate within matrix grains, which display as deformed grains or DRX grains. A similar phenomenon also appears in the research by Zong et al. [19]. By the orientation deviation measurement of matrix grains, the twin boundary analysis, and the TEM study, Zong et al. [19] concluded that the grains with 89 ± 3° GBs were related to DDRX. Many previous studies have proven the occurrence of DDRX in TiAl alloy [21–23]. DDRX dominates the nucleation and growth of recrystallized grains through the bulge and migration of HAGBs, as shown in Fig. 8. Previous studies reported that the nucleation sites of DDRXed grains are mainly at grain boundaries, subgrain boundaries, and twin boundaries, especially at triple junctions, as exhibited in Fig. 8b. Because the intense dislocation movement around the grain boundary can provide higher energy and promote the nucleation and growth of DDRXed grains [19, 24, 25]. Moreover, the nucleation time of DRXed grains is different, while the original grain boundaries and twin boundaries transform to HAGBs with random distribution during the loading. Therefore, the orientation of DDRXed grains will be different from the orientation of original grains [24]. Crystal orientation schematic diagrams and Euler angles of small grains with 89 ± 3° GBs in deformed grains (marked by green grains) and DRX grains (marked by blue grains) are exhibited in Fig. 7. It can be seen that the crystal orientation of grain *B* is completely different from matrix grain *A* (deformed grain), and the crystal orientation of grain *C* is also completely different from matrix grain *D* (recrystallized grain). Therefore, it is speculated that DDRX produces the tiny grains with 89 ± 3° GBs.

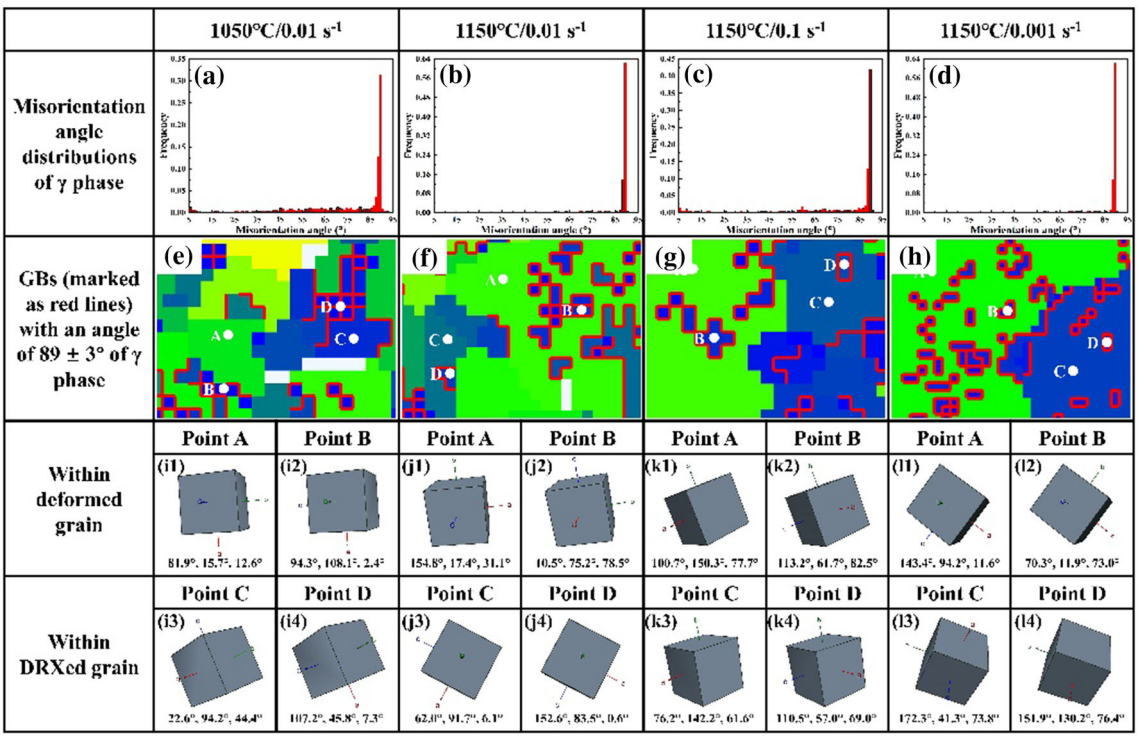

Figure 7 Misorientation angle distribution **a**, **b**, **c**, **d**, 89 ± 3° GBs distribution diagram **e**, **f**, **g**, **h** and crystal orientation diagram inside **i**, **j**, **k**, **l** the grains of γ phase in various conditions.

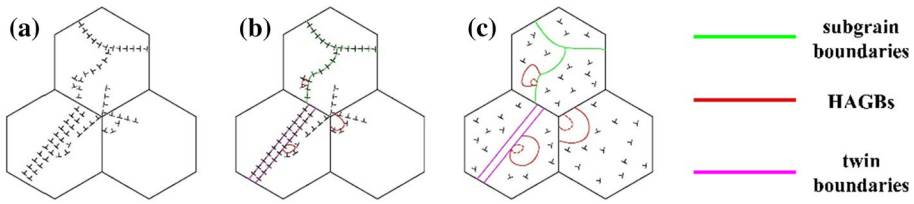

Figure 8 The schematic diagram of discontinuous dynamic recrystallization mechanism.

In contrast to DDRX, CDRX generally occurs within the grains. Figure 9 shows a nucleation and growth mechanism for the grains with CDRX, which is considered to be an intense recovery process. During the loading, sub-grain boundaries continuously absorb dislocations, which lead to increasing misorientation of sub-grain boundaries, and result in continuous rotation of sub-grains [26–29]. With further deformation, the sub-grain boundaries with low angle gradually transform into HAGBs, and the sub-grains also become independent recrystallized grains [30]. Because CDRX will lead to local rotation and orientation difference to result in orientation gradients within the grains [24]. As shown in Fig. 10, large grains with gradient colors were present in various samples. Different colors in the grains indicate the differences between the orientation groups of the crystals. The crystal orientation accumulation curves along the line from point *O* to point *A* in the deformed grains were measured. From the curves, it can be seen that the orientation accumulation pattern is a typical orientation jumping pattern. And the accumulated misorientation is all greater than 15°. Additionally, when direct misorientation angle of grain boundary represents at 10–15°, grains nucleation with CDRX can be carried out by sub-grain rotation [31, 32]. In summary, two types of dynamic recrystallization mechanism, DDRX, and CDRX, appear during the isothermal deformation.

The variety of grain orientation

Figure 11 shows the inverse pole figure (IPF) maps of matrix unit in various conditions. The inverse polar figure shows the statistical results about the crystal orientation of γ-phase grains. Obviously, dynamic recrystallization happens in various conditions, but recrystallized grains will be much smaller at low temperature or high strain rate. The point with higher pole densities (red dots) in the inverse pole figure is considered to be possible preferred orientation of grains [24]. It can be seen that the point gradually rotates in $< 010 >$ direction with the temperature increasing or the strain rate decreasing in Fig. 11. The polar figures of deformed samples in various conditions are shown in Fig. 12. The comparison of texture in condition 1150 °C/0.1 s^{-1} and 1150 °C/0.001 s^{-1} are exhibited in Fig. 12c and d. By comparison of (100), (110), and (111) polar figures, it can be found that distribution of texture tends to be scattered in condition 1150 °C/0.1 s^{-1}. With the strain rate decreasing to 0.001 s^{-1}, the scattered texture transforms to be a texture with high strength. The peak intensity of polar graph in Fig. 12d is twice as strong as that in Fig. 12c. Similarly, with the temperature increasing to 1150 °C, the texture of γ-phase transforms from scattered to concentrated at the same strain rate.

According to recent researches [24, 28, 29], when CDRX mechanism dominates the deformation, a

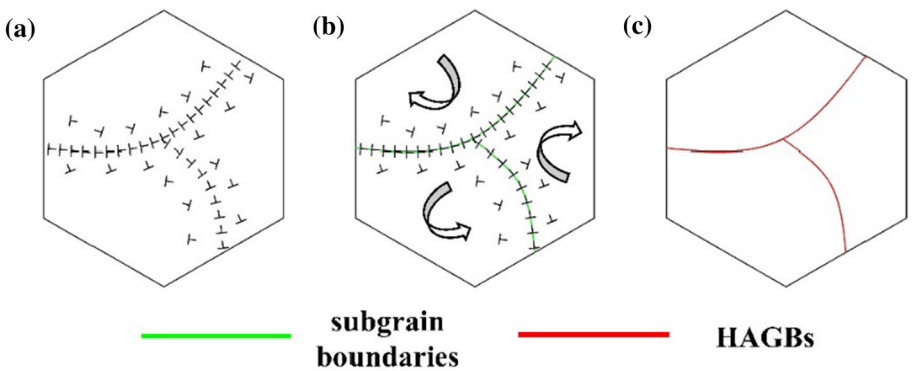

Figure 9 The schematic diagram of continuous dynamic recrystallization mechanism.

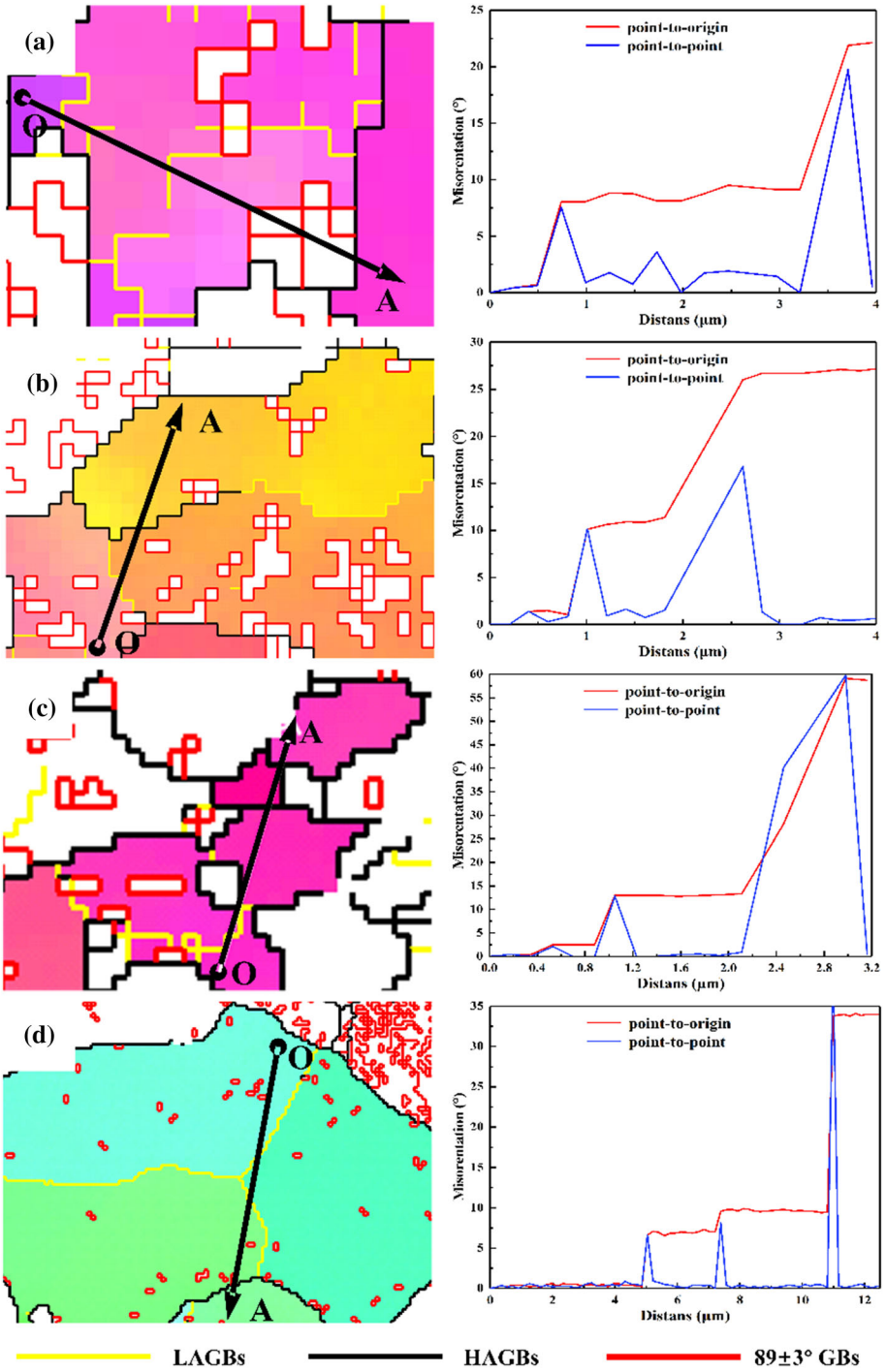

Figure 10 The orientation maps and the misorientation measurement along the black line of γ phase after isothermal compression in condition 1050 °C/0.01 s^{-1} **a**, 1150 °C/0.01 s^{-1} **b**, 1150 °C/0.1 s^{-1} **c** and 1150 °C/0.001 s^{-1} **d**.

texture with high strength occurs in condition with large strain. Although CDRX, characterized by sub-grain rotation, slightly changes the orientation of sub-grains, the deformation mechanism of sub-grains and parent grains is the same. It will cause the same direction rotation between sub-grains and parent grains [33, 34]. Even if the sub-grain formation might cause the orientation difference, sub-grains and parent grains will still tend to be the same component of texture. When DDRX becomes the dominant deformation mechanism, the concentrated texture might not appear. It mainly results from a large difference between the crystal orientations of DDRXed grains and the original grains. Thus, two reasons might be

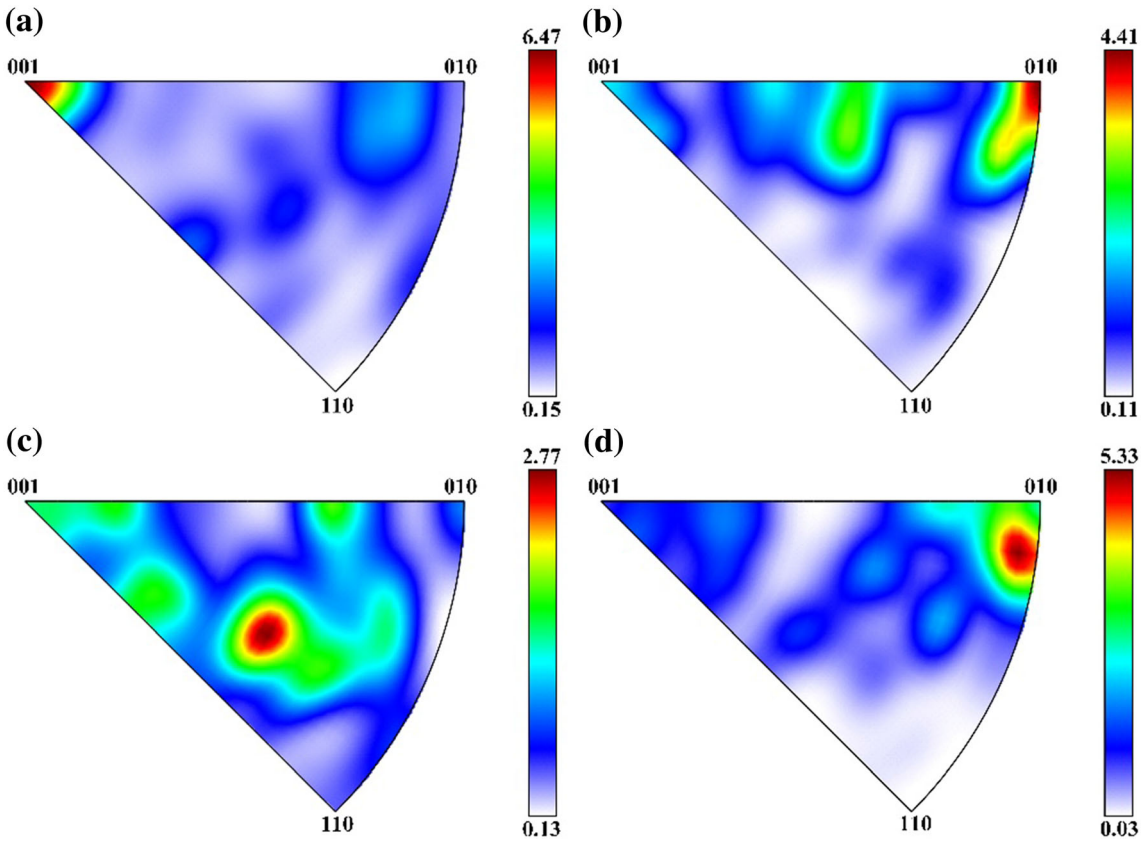

Figure 11 Inverse pole figures (// Compression direction) of γ phase after isothermal compression in condition 1050 °C/0.01 s^{-1} **a**, 1150 °C/0.01 s^{-1} **b**, 1150 °C/0.1 s^{-1} **c** and 1150 °C/0.001 s^{-1} **d**.

suggested for the texture evolution during the deformation. (1) At low temperatures or high strain rates, the recrystallized grains do not grow, the volume fraction of recrystallized grains is small, and the texture mainly influenced by deformed grains tends to be scattered. With the temperature increasing or/and the strain rate decreasing, recrystallized grains grow significantly. The texture mainly influenced by the nucleation and growth of recrystallized grains tends to be concentrated. (2) At lower temperatures or higher strain rates, the dynamic recrystallization mechanism might be dominated by DDRX, which results in scattered texture. With the strain rate decreasing, the dominant mechanism of dynamic recrystallization changes from DDRX to CDRX, which leads to a concentrated texture.

Conclusions

In this paper, ($\alpha_2 + \gamma$) lamellar colonies occur within the matrix units of the present composites, while the size of the lamellar colonies in the center of matrix unit is much larger than that in the edge of matrix unit. The reinforcements distribute as a network structure in the interface layer of matrix units. After the isothermal compression, most reinforcements are perpendicular to the compressive direction. The main conclusions are listed as follows.

1. A large number of recrystallized grains with 89 ± 3° GBs appear in the γ phase within the matrix units during the loading. The nucleation and growth of discontinuous dynamic recrystallized grains are usually dominated by the HAGB migration at grain boundaries, sub-grain boundaries, and twin boundaries. The sub-grain boundaries within deformed grains provide nucleation sites for DDRX. Additionally, sub-grain boundaries lead to dislocation pile-ups, which provide

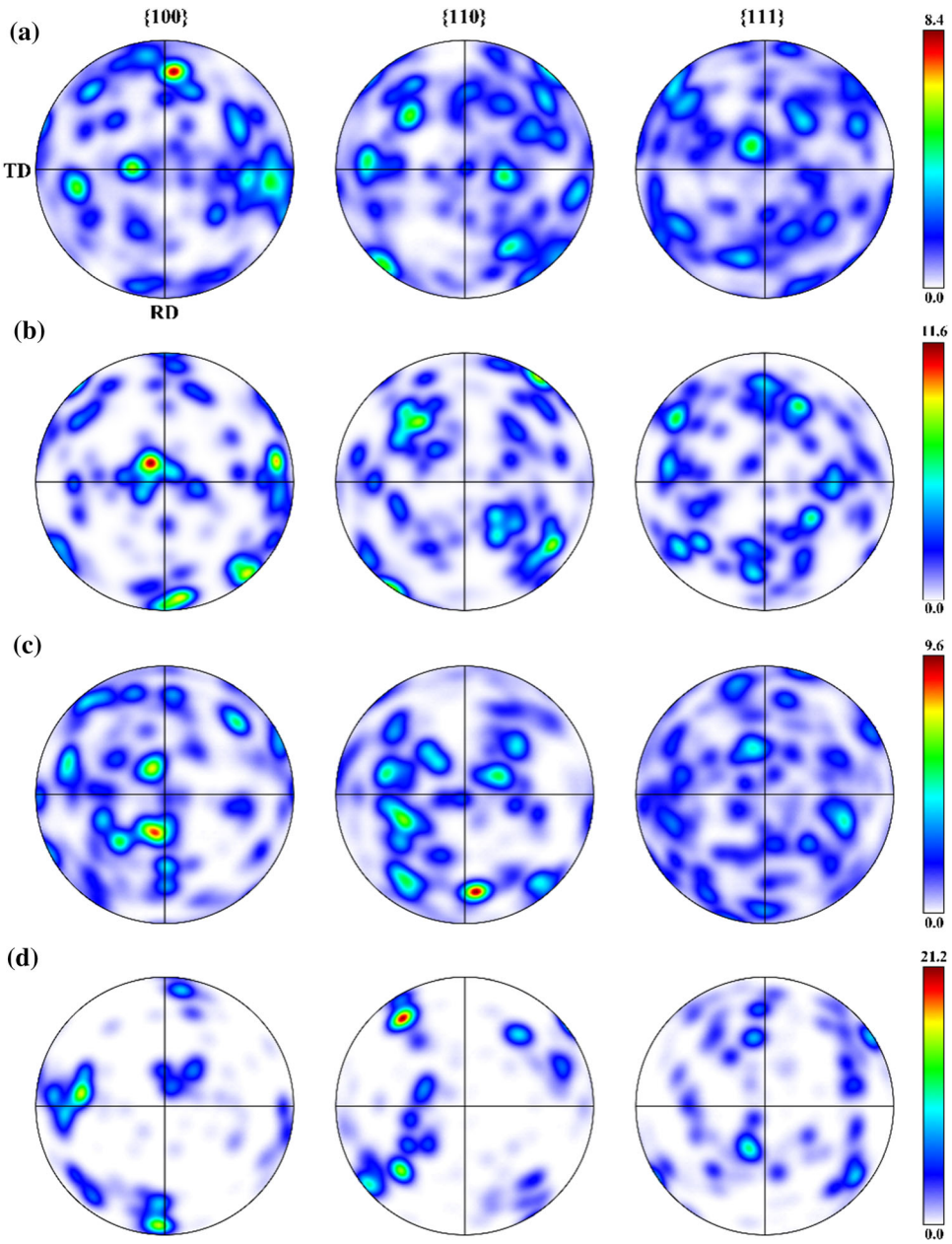

Figure 12 Pole figures of γ phase for the alloy after isothermal compression in condition 1050 °C/0.01 s^{-1} **a**, 1150 °C/0.01 s^{-1} **b**, 1150 °C/0.1 s^{-1} **c** and 1150 °C/0.001 s^{-1} **d**.

sufficient energy for nucleation and growth of recrystallized grains with DDRX.

2. Continuous dynamic recrystallization within the deformed grains is mainly caused by the sub-grain rotation within the matrix units. It is generally dominated by the accumulation and entanglement of dislocations, the formation of sub-grain boundaries and the transformation from sub-grain boundaries to HAGBs. The orientation accumulation is the typical directional jump pattern, while the accumulated misorientation all exceeds 15°. It indicates the existence of continuous dynamic recrystallization within the matrix units.
3. With the temperature increasing and the strain rate decreasing, <010> direction of γ-phase grains gradually tends to be parallel to compressive direction, and texture changes from scattered to concentrated. With the volume fraction of recrystallized grains increasing, the crystal orientation primarily is influenced by the orientation of recrystallized grains. Additionally, the continuous dynamic recrystallization might lead to a concentrated texture during the loading.

Acknowledgements

This study was supported by the National Natural Science Foundation of China (52101034), the Postdoctoral Project of Chongqing Natural Science Foundation (cstc2021jcyj-bshX0067), the Scientific and Technological Research Program of Chongqing Municipal Education Commission (KJQN202101138) and the Scientific Research Foundation of Chongqing University of Technology (2020ZDZ003).

Declarations

Conflict of interest The authors declare that there are not any financial and personal relationships with other people or organizations that could inappropriately influence our work or state. There are no professional or other personal interests of any nature or kind in any product, service, or company that could be constructed as influencing the position presented in or the review of the manuscript.

References

[1] Clemens H, Mayer S (2013) Design, processing, microstructure, properties, and applications of advanced intermetallic TiAl alloys. Adv Eng Mater 15(4):191–215. https://doi.org/10.1002/adem.201200231

[2] Ding J, Zhang MH, Liang YF, Ren Y, Dong CL, Lin JP (2018) Enhanced high-temperature tensile property by gradient twin structure of duplex high-Nb-containing TiAl alloy. Acta Mater 161:1–11. https://doi.org/10.1016/j.actamat.2018.09.007

[3] Kim YW, Kim SL (2018) Advances in gammalloy materials–processes–application technology: successes, dilemmas, and future. JOM 70(4):553–560. https://doi.org/10.1007/s11837-018-2747-x

[4] Dimiduk DM (1999) Gamma titanium aluminide alloys: an assessment within the competition of aerospace structural materials. Mater Sci Eng A 263:281–288. https://doi.org/10.1016/S0921-5093(98)01158-7

[5] Liang XP, Liu ZQ, Li HZ, Chen FH, Yang WF, Ouyang SH, Liu Y, Wang L (2020) Microstructure and elevated-temperature mechanical properties of in situ Ti_2AlNb-reinforced TiAl-matrix composite prepared by powder metallurgy. Mater Today Commun. https://doi.org/10.1016/j.mtcomm.2020.101179

[6] Wang DQ, Sun DL, Han XL, Wang Q (2019) In situ Ti_2AlN reinforced TiAl-based composite with a novel network structure: Microstructure and flexural property at elevated temperatures. Mater Sci Eng A 742:231–240. https://doi.org/10.1016/j.msea.2018.11.018

[7] Zhou Y, Sun DL, Jiang DP, Han XL, Wang Q, Wu GH (2013) Microstructural characteristics and evolution of Ti_2AlN/TiAl composites with a network reinforcement architecture during reaction hot pressing process. Mater Charact 80:28–35. https://doi.org/10.1016/j.matchar.2013.03.007

[8] Xiao SL, Guo YF, Liang ZQ, Wang XA, Yang JK, Wang X, Xu LJ, Tian J, Chen YY (2020) The effect of nano-Y_2O_3 addition on tensile properties and creep behavior of as-cast TiAl alloy. J Alloys Compd. https://doi.org/10.1016/j.jallcom.2020.153852

[9] Guo YF, Xiao SL, Chen YY, Tian J, Zheng ZZ, Xu LJ (2020) High temperature tensile properties and fracture behavior of Y_2O_3-bearing Ti–48Al–2Cr–2Nb alloy. Intermetallics. https://doi.org/10.1016/j.intermet.2020.106933

[10] Li MA, Xiao SL, Chen YY, Xu LJ, Tian J (2019) The effect of carbon addition on the high-temperature properties of β solidification TiAl alloys. J Alloys Compd 775:441–448. https://doi.org/10.1016/j.jallcom.2018.09.397

[11] Ren LR, Qin SJ, Zhao SH, Xiao HQ (2021) Fabrication and mechanical properties of Ti_2AlC/TiAl composites with co-continuous network structure. T Nonferr Metal Soc 31(7):2005–2012. https://doi.org/10.1016/S1003-6326(21)65633-9

[12] Li MA, Xiao SL, Chen YY, Xu LJ, Tian J (2018) The effect of boron addition on the high-temperature properties and microstructure evolution of high Nb containing TiAl alloys. Mater Sci Eng A 733:190–198. https://doi.org/10.1016/j.msea.2018.07.019

[13] Li AB, Cui XP, Wang GS, Qu W, Li F, Zhang XX, Gan WC, Geng L, Meng SH (2016) Fabrication of in situ Ti_5Si_3/TiAl composites with controlled quasi-network architecture using reactive infiltration. Mater Lett 185:351–354. https://doi.org/10.1016/j.matlet.2016.09.015

[14] Cheng L, Chang H, Tang B, Kou HC, Li JS (2013) Deformation and dynamic recrystallization behavior of a high Nb containing TiAl alloy. J Alloys Compd 552:363–369. https://doi.org/10.1016/j.jallcom.2012.11.076

[15] Li MA, Li J, Zhou T, Xiao SL, Chen YY, Xu LJ, Hu L, Shi LX (2021) The investigation of microstructure evolution, deformation behavior and processing performance of the high niobium containing TiAl alloys. Intermetallics. https://doi.org/10.1016/j.intermet.2021.107336

[16] Tian SW, He AR, Liu JH, Zhang YF, Zhang SY, Zhang Y, Yang YG, Jiang HT (2021) Investigation on the microstructure evolution and dynamic recrystallization mechanisms of TiAl alloy at elevated temperature. J Mater Res Technol 14:968–984. https://doi.org/10.1016/j.jmrt.2021.06.107

[17] Dong SL, Chen RR, Guo JJ, Ding HS, Su YQ, Fu HZ (2015) Deformation behavior and microstructural evolution of directionally solidified TiAlNb-based alloy during thermo-compression at 1373–1573 K. Mater Des 84:118–132. https://doi.org/10.1016/j.matdes.2015.06.117

[18] Zhang HB, Zhang KF, Zhou HP, Lu Z, Zhao CH, Yang XL (2015) Effect of strain rate on microstructure evolution of a nickel-based superalloy during hot deformation. Mater Des 80:51–62. https://doi.org/10.1016/j.matdes.2015.05.004

[19] Zong YY, Wen DS, Liu ZY, Shan DB (2016) γ-Phase transformation, dynamic recrystallization and texture of a forged TiAl-based alloy based on plane strain compression at elevated temperature. Mater Des 91:321–330. https://doi.org/10.1016/j.matdes.2015.11.120

[20] Wang QP, Zhou RF, Li YK, Geng BY (2020) Characteristics of dynamic recrystallization in semi-solid CuSn10P1 alloy during hot deformation. Mater Charact. https://doi.org/10.1016/j.matchar.2019.109996

[21] Wang QB, Zhang SZ, Zhang CJ, Zhang WG, Yang JR, Duo D, Zhu DD (2021) The influence of the dynamic softening mechanism of α phase and γ phase on remnant lamellae during hot deformation. J Alloys Compd. https://doi.org/10.1016/j.jallcom.2021.159514

[22] Chen XF, Tang B, Liu Y, Xue XY, Li L, Kou HC, Li JS (2019) Dynamic recrystallization behavior of the Ti–48Al–2Cr–2Nb alloy during isothermal hot deformation. Prog Nat Sci 29(5):587–594. https://doi.org/10.1016/j.pnsc.2019.08.004

[23] Wan ZP, Sun Y, Hu LX, Yu H (2017) Experimental study and numerical simulation of dynamic recrystallization behavior of TiAl-based alloy. Mater Des 122:11–20. https://doi.org/10.1016/j.matdes.2017.02.088

[24] Chen XF, Tang B, Liu D, Wei BB, Zhu L, Liu RC, Kou HC, Li JS (2021) Dynamic recrystallization and hot processing map of Ti–48Al–2Cr–2Nb alloy during the hot deformation. Mater Charact. https://doi.org/10.1016/j.matchar.2021.111332

[25] Zhong XT, Wang L, Huang LK, Liu F (2020) Transition of dynamic recrystallization mechanism during hot deformation of Incoloy 028 alloy. J Mater Sci Technol 42:241–253. https://doi.org/10.1016/j.jmst.2019.08.058

[26] Xiang L, Tang B, Xue XY, Kou HC, Li JS (2018) Microstructural characteristics and dynamic recrystallization behavior of β–γ TiAl based alloy during high temperature deformation. Intermetallics 97:52–57. https://doi.org/10.1016/j.intermet.2018.04.002

[27] Luo R, Chen L, Zhang YX, Cao Y, Peng CT, Yang YY, Liu T, Zheng Q, Cheng XN (2021) Characteristic and mechanism of dynamic recrystallization in a newly developed Fe–Cr–Ni–Al–Nb superalloy during hot deformation. J Alloys Compd. https://doi.org/10.1016/j.jallcom.2021.158601

[28] Gourdet S, Montheillet F (2003) A model of continuous dynamic recrystallization. Acta Mater 51(9):2685–2699. https://doi.org/10.1016/S1359-6454(03)00078-8

[29] Huang K, Logé RE (2016) A review of dynamic recrystallization phenomena in metallic materials. Mater Des 111:548–574. https://doi.org/10.1016/j.matdes.2016.09.012

[30] Sakai T, Belyakov A, Kaibyshev R, Miura H, Jonas JJ (2014) Dynamic and post-dynamic recrystallization under hot, cold and severe plastic deformation conditions. Prog Mater Sci 60:130–207. https://doi.org/10.1016/j.pmatsci.2013.09.002

[31] Li DF, Guo QM, Guo SL, Peng HJ, Wu ZG (2011) The microstructure evolution and nucleation mechanisms of dynamic recrystallization in hot-deformed Inconel 625 superalloy. Mater Des 32(2):696–705. https://doi.org/10.1016/j.matdes.2010.07.040

[32] Pongea D, Gottsteina G (1998) Necklace formation during dynamic recrystallization: mechanisms and impact on flow behavior. Acta Mater 46(1):69–80. https://doi.org/10.1016/S1359-6454(97)00233-4

[33] Tóth LS, Estrin Y, Lapovok R, Gu CF (2010) A model of grain fragmentation based on lattice curvature. Acta Mater 58(5):1782–1794. https://doi.org/10.1016/j.actamat.2009.11.020

[34] Gourdet S, Montheillet F (2000) An experimental study of the recrystallization mechanism during hot deformation of aluminium. Mater Sci Eng A 283(1–2):274–288. https://doi.org/10.1016/S0921-5093(00)00733-4